

Phase Perfection in Zinc Blende and Wurtzite III–V Nanowires Using Basic Growth Parameters

Hannah J. Joyce,* Jennifer Wong-Leung, Qiang Gao, H. Hoe Tan, and Chennupati Jagadish

Department of Electronic Materials Engineering, Research School of Physics and Engineering, The Australian National University, Canberra, ACT 0200, Australia

ABSTRACT Controlling the crystallographic phase purity of III–V nanowires is notoriously difficult, yet this is essential for future nanowire devices. Reported methods for controlling nanowire phase require dopant addition, or a restricted choice of nanowire diameter, and only rarely yield a pure phase. Here we demonstrate that phase-perfect nanowires, of arbitrary diameter, can be achieved simply by tailoring basic growth parameters: temperature and V/III ratio. Phase purity is achieved without sacrificing important specifications of diameter and dopant levels. Pure zinc blende nanowires, free of twin defects, were achieved using a low growth temperature coupled with a high V/III ratio. Conversely, a high growth temperature coupled with a low V/III ratio produced pure wurtzite nanowires free of stacking faults. We present a comprehensive nucleation model to explain the formation of these markedly different crystal phases under these growth conditions. Critical to achieving phase purity are changes in surface energy of the nanowire side facets, which in turn are controlled by the basic growth parameters of temperature and V/III ratio. This ability to tune crystal structure between twin-free zinc blende and stacking-fault-free wurtzite not only will enhance the performance of nanowire devices, but also opens new possibilities for engineering nanowire devices, without restrictions on nanowire diameters or doping.

KEYWORDS Nanowire, electron microscopy, zinc blende, wurtzite, growth

Semiconductor nanowires are predicted to be key components of future devices and systems. Offering reduced dimensionality, outstanding materials properties, and the capability for bottom-up assembly, these nanostructures are highly promising nanobuilding blocks. Nanowire-based devices, such as solar cells,^{1,2} lasers,^{3,4} photodetectors,⁵ integrated photonic circuits,⁶ and highly sensitive biological and chemical sensors⁷ have already been developed. Several of these devices were created using III–V nanowires.^{2,4,5} III–V nanowires are ideal for photonic devices due to their direct band gap and superior electrical properties. Furthermore, III–V nanowires can be grown epitaxially on Si, which enables III–V nanowire optoelectronic devices to be integrated with established Si microelectronics technology.⁸

Despite significant advances in nanowire growth, the crystallographic quality of nanowires remains difficult to control. The cubic zinc blende (ZB) phase, which is the stable phase in bulk III–V materials, is not always the dominant phase in nanowires. Instead, nanowires often feature the hexagonal wurtzite (WZ) phase in sections of, or throughout, the nanowire. Twin defects, stacking faults, and ZB–WZ polytypism are commonly reported problems. Several studies have demonstrated that these defects adversely impact the optical and electronic properties of III–V nanowires, for instance, by reducing the quantum efficiency, carrier life-

time, and carrier mobility.⁹ Device applications demand nanowires with excellent physical properties, and consequently, control over the nanowire crystal structure is imperative. On the other hand, controlled twin planes, stacking faults, and polytypism offer new possibilities for engineering nanowire band structure, luminescence polarization, and emission energy.¹⁰

Research into controlling nanowire crystal structure has intensified. Several reports address the diameter dependency of nanowire crystal structure, with smaller diameter nanowires tending toward a WZ phase and larger diameter nanowires tending toward a ZB phase.^{11–13} Algra et al. observed a dramatic transition from a WZ structure to a periodically twinned ZB structure upon the addition of Zn dopants to the InP nanowire growth system.¹² Caroff et al. used a combination of nanowire diameter and growth temperature to controllably achieve WZ and periodically twinned ZB InAs nanowires.¹³

The aforementioned methods for controlling crystal phase necessitate a particular choice of nanowire diameter or the deliberate introduction of dopants. Arguably, nanowire diameter and doping can change nanowire properties as dramatically as crystallographic phase itself. For device applications, it is desirable to control crystal quality without sacrificing important specifications of diameter and dopant levels. Furthermore, these methods seldom produced truly phase-perfect nanowires free of twin defects and stacking faults.

* Corresponding author, hjj109@physics.anu.edu.au.

Received for review: 11/4/2009

Published on Web: 02/04/2010

Fortunately, two basic growth parameters have exhibited potential as a means to control crystal phase. These basic parameters are, first, growth temperature and, second, the ratio of the group V precursor flow rate to the group III precursor flow rate, termed the V/III ratio. Increasing the growth temperature is known to promote twin defect formation in GaP¹⁴ and GaAs^{13,15} nanowires. Increasing the second parameter, V/III ratio, is known to reduce the occurrence of twin defects in GaAs nanowires.¹⁶

In this study, we vary only these two basic growth parameters, to achieve III–V nanowires in either perfect WZ or ZB form. This method affords precise control over nanowire crystal structure, using only basic growth parameters without limiting diameter choice or requiring dopant addition. We demonstrate that for a given diameter, both WZ and ZB nanowires can be grown without stacking faults or twin defects. Furthermore, to the best of our knowledge, this is the first report of twin-free ZB InAs nanowires.

By identifying the growth conditions that dictate nanowire growth, we gain much insight into the mechanisms of WZ and ZB growth and planar defect formation. In this article, we develop a theoretical model, based on classical nucleation theory, to support these mechanisms. Several studies advocate nucleation theory for the study of WZ and ZB formation in nanowire and bulk systems.^{14,17–19} Glas et al.¹⁸ have developed a robust nucleation model which first predicts nucleus formation at the vapor–liquid–solid triple-phase boundary, and second predicts WZ nanowires at high supersaturation growth conditions. Johansson et al.^{14,19} and Algra et al.¹² have developed useful nucleation models to explain the formation of WZ nanowires and periodically twinned ZB nanowires. Our model builds on these pre-existing models to describe the effect of temperature and V/III ratio on nanowire crystal structure. Importantly, our results and theoretical analysis reveal that changes to the surface energy at the nanowire nucleus–vapor interface, brought about by changes in temperature and V/III ratio, are crucial for the ZB–WZ phase transition.

InAs nanowires were grown via horizontal flow metalorganic chemical vapor deposition (MOCVD) using trimethylindium (TMI) as the group III precursor and AsH₃ as the group V precursor, and Au nanoparticles to drive nanowire growth. InAs(111)B substrates were treated with poly-L-lysine solution followed by a solution of colloidal Au nanoparticles 50 nm in diameter. Nanowires were grown at a pressure of 100 mbar and a total gas flow rate of 15 slm. Prior to growth, each substrate was annealed in situ at 600 °C under AsH₃ ambient to desorb surface contaminants. After the substrate cooled to growth temperature, the AsH₃ flow was adjusted and TMI was introduced to initiate nanowire growth. The growth time was 30 min for each sample. The group III (TMI) flow rate was 1.2×10^{-5} mol/min for all growths. We studied growth temperatures between 375 and 550 °C. To study V/III ratio, AsH₃ flow rates were chosen between 1.7×10^{-5} and 4.1×10^{-3} mol/min to attain V/III

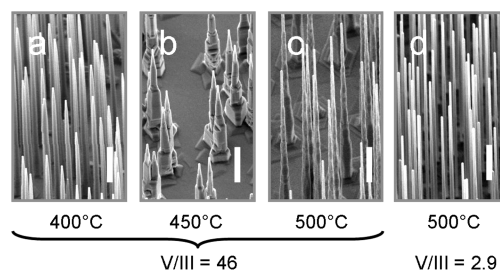


FIGURE 1. FESEM images of InAs nanowires. Nanowires were grown at temperatures between 400 and 500 °C, with V/III ratios as indicated. Scale bar is 1 μm. Samples are tilted at 40°.

ratios between 1.4 and 370, varying in binary orders of magnitude. InAs nanowires grown under various temperature and V/III conditions were characterized by field emission scanning electron microscopy (FESEM) and transmission electron microscopy (TEM). Adjunct studies of GaAs nanowire growth, and studies using different Au nanoparticle diameters (10, 20, 30, and 100 nm), were performed to demonstrate the applicability of our results to other nanowire diameters and to III–V materials other than InAs. These additional results are presented in section S2 of the Supporting Information.

FESEM (Hitachi 4500) investigations were carried out at an accelerating voltage of 3 kV. FESEM analysis was used to identify the general morphology of the nanowires such as facet planes, diameter, and height. Figure 1 illustrates FESEM images of typical nanowires grown at different temperatures and V/III ratios. Nanowires generally grew normal to the (111)B substrate, indicating the nanowires have a [111] or [0001] orientation defined by whether they were ZB or WZ, respectively. InAs nanowire growth occurred in a limited range of temperatures and V/III ratios, consistent with previous studies of III–V nanowires.²⁰ We examined the crystal structure of nanowires throughout this range.

For TEM investigations, nanowires were mechanically transferred to holey carbon grids and analyzed using a Phillips CM300 TEM operated at 300 kV. Conventional bright field and dark field TEM imaging of the nanowires along the [110]/[1120] zone axis was used to identify the crystal structures, twin phase boundaries, and stacking faults, in combination with selected area diffraction and lattice imaging. To ensure consistency and reproducibility, at least three nanowires from each sample were examined in detail. Key growths were duplicated, and at least 10 nanowires were examined in such cases. Nanowires were screened for twin defects and stacking faults over their entire length. The composition of the Au nanoparticle was studied by energy dispersive X-ray (EDX) analysis.

Figure 2 illustrates high-resolution TEM (HRTEM) and selected area diffraction patterns (SADP) of InAs nanowires grown at the lower (400 °C), middle (450 °C), and upper (500 °C) temperatures of the growth window. At 400 °C (Figure 2a), the nanowires are pure ZB without planar crystallographic defects. The SADP in Figure 2e consists of

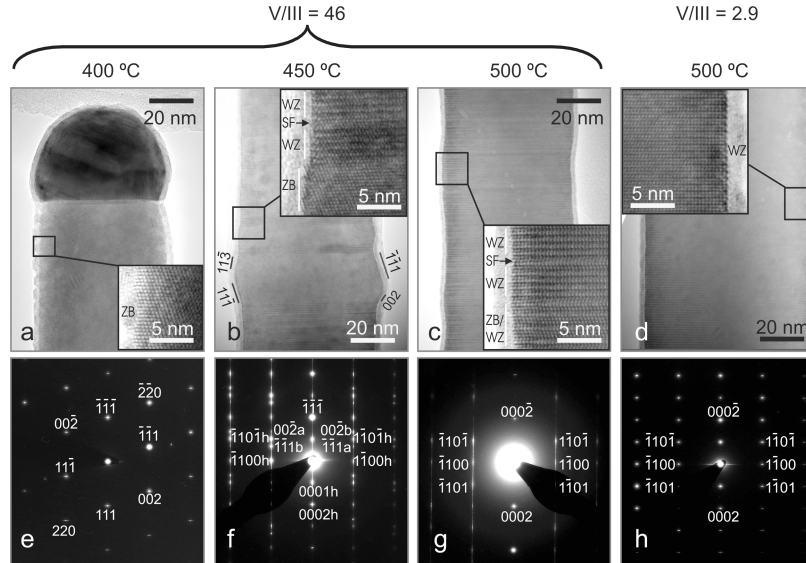


FIGURE 2. TEM results for InAs nanowires. (a–d) HRTEM images of nanowires grown at the indicated temperatures and V/III ratios, and (e–h) their respective SADP. The insets in (a–d) show higher magnification images with ZB and WZ regions, and stacking faults (SF) labeled. The indexed SADP patterns illustrate the nanowires are (e) twin-free ZB, (f) mixed ZB (spots denoted “a” and “b”) and WZ (spots denoted “h”) with stacking faults and twin defects, (g) WZ with stacking faults, and (h) stacking fault-free WZ.

a single set of diffraction spots characteristic of a twin-free ZB crystal. At the higher growth temperature of 450 °C (Figure 2b), the nanowires feature a mixture of WZ and ZB segments. The diffraction pattern (Figure 2f) is a superposition of WZ and ZB diffraction patterns. Certain ZB diffraction spots appear as doublets, for instance, (002)^a and (111)^b. This is indicative of rotational twins (as denoted by a and b) in the [111] growth direction which give superimposed diffraction patterns along the ⟨110⟩ direction.

At the highest growth temperature, 500 °C, nanowires have a predominantly WZ structure (Figure 2c). The diffraction pattern (Figure 2g) is characteristic of WZ crystal, and streaks in the [0001] direction indicate the presence of stacking faults along the (0001̄) growth plane. HRTEM reveals that thin ZB segments, up to six bilayers thick, are also present. Note that the diffraction pattern does not reveal this minority ZB phase due to the high contrast streaks arising from the stacking faults.

Here, it is important to understand the definitions of ZB, WZ, twins, and stacking faults. ZB sections follow an ABCABC stacking sequence, whereas WZ sections follow an ABABAB stacking sequence. Each letter represents a bilayer of III–V pairs as described in section S3 of the Supporting Information. In a WZ structure, a stacking fault occurs when a single bilayer is misplaced, locally creating a ZB stacking sequence. For instance, sequence ABABCBCB, growing from left to right, features a faultily placed bilayer at C. This creates a minimally thin ZB segment, ABC. A twin plane defect occurs when a single bilayer is faultily stacked in a ZB crystal, which reverses the stacking sequence from ABC to CBA. For example, in a section ABCABA_ACBA, growing from left to right, A is the faultily stacked bilayer creating the twin plane. We denote A the “twinned bilayer”. This creates a minimally

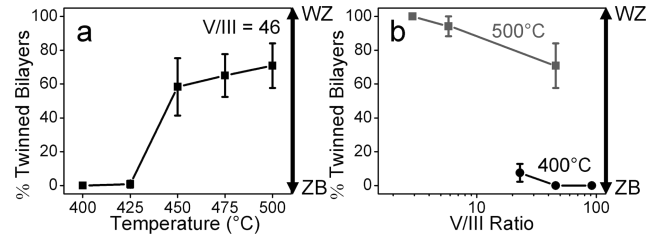


FIGURE 3. Percentage of twinned bilayers. Nanowires were grown at (a) different temperatures and a V/III ratio of 46, and (b) different V/III ratios, with constant growth temperatures of 400 °C (black) and 500 °C (gray). Error bars represent the standard deviation over 10 segments of nanowire, each segment 20 bilayers thick.

thin WZ segment ABAA. Sequential twin planes, or equivalently sequential twinned bilayers, create an extended WZ structure. As the proportion of twinned bilayers increases from 0 to 100 %, the crystal phase changes from ZB to WZ. In Figure 3, the proportion of twinned bilayers is quantified for different growth temperatures and V/III ratios. These data were determined by examining HRTEM images and counting the number of twinned bilayers per segment of 20 bilayers. For each data point we analyzed 10 segments, each 20 bilayers thick. These segments were chosen randomly from at least four HRTEM images obtained from at least two different nanowires. Figure 3a clearly illustrates that as growth temperature is increased, the nanowire makes a transition from ZB to WZ.

Next, we examine the V/III ratio and find it has a remarkable effect on crystal structure. A high V/III ratio promotes a ZB phase whereas a low V/III ratio promotes a WZ phase. This trend is clear in Figure 3b, which plots the proportion of twinned bilayers in nanowires grown at different V/III ratios.

For example, compare the predominantly WZ nanowires of panels c and d of Figure 2 with a common growth temperature of 500 °C. The nanowires grown at a higher V/III ratio of 46 (Figure 2c) have a high density of stacking faults and some thin ZB sections. The nanowires grown with a significantly lower V/III ratio of 2.9 (Figure 2d), in contrast, were pure WZ and free of stacking faults. Clearly, a low V/III ratio reduces stacking faults and promotes a perfect WZ phase. Only a thin, less than 40 nm thick, neck region at the nanowire tip, directly below the nanoparticle, shows any degree of polytypism. The neck region is formed during postgrowth cooling,²¹ rather than during growth, so it is omitted from the quantitative analyses of Figure 3.

By a combination of a high growth temperature and low V/III ratio, pure WZ nanowires, as in Figure 2d, were obtained. These nanowires complement the pure ZB nanowires of Figure 2a grown at the low temperature of 400 °C and high V/III ratio of 46. Thus two basic parameters, namely, growth temperature and V/III ratio, afford precise control over the nanowire crystal phase. To further demonstrate this ability to control crystal phase over the entire nanowire length, section S1 of the Supporting Information presents bright field TEM images of typical ZB and WZ nanowires, along with HRTEM and SADP taken at multiple points along the nanowire length.

Furthermore, pure ZB and pure WZ nanowires could be achieved across the wide range of nanowire diameters investigated. Section S2 of the Supporting Information presents TEM results for nanowires catalyzed by Au nanoparticles of diameter 10–100 nm. For both narrow and wide nanowire diameters, twin-free ZB nanowires could be achieved using low temperature and high V/III ratio, and stacking fault-free WZ nanowires could be achieved using the opposite conditions.

Moreover, these results translate to III–V material systems other than InAs. For example, using the same principles, GaAs nanowires could be tailored between twin-free ZB and perfect WZ, over a wide range of nanowire diameters. TEM results for GaAs nanowires are detailed in section S2 of the Supporting Information.

To develop a physical explanation for the ZB–WZ phase control demonstrated, we require information about the sidewall facets adopted under different growth conditions. Certainly, growth temperature and V/III ratio can have a significant effect on the thermodynamic stability of sidewall facets, as on nanowire crystal phase.²²

SEM and TEM were used to determine the sidewall facets. Using SEM, we indexed the sidewall facets against the {110} cleavage planes of the substrate. Using TEM, we studied short (<500 nm long) sections of nanowire and imaged their cross sections along the ⟨111⟩⟨0001⟩ zone axis. We also imaged full nanowire lengths along the ⟨110⟩⟨1120⟩ and ⟨112⟩⟨1100⟩ zone axes. By indexing these TEM images against their corresponding SADP, we confirmed the sidewall indices.

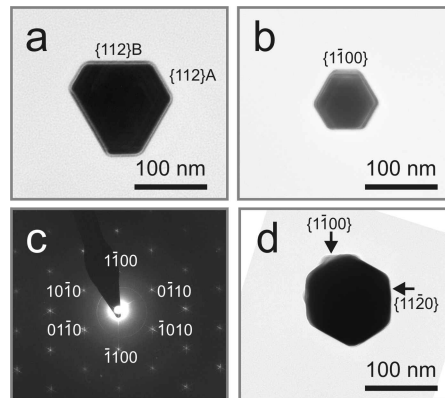


FIGURE 4. Bright field TEM and SADP of nanowire cross sections taken along the [111] zone axis. (a, b) Mixed ZB/WZ nanowire grown at 450 °C with {112}/{1100} facets. (c) SADP pattern corresponding to image (b). (d) WZ nanowire grown at 500 °C with {1120} facets at the base and {1100} facets at the tip.

Consistent with previous studies of III–V nanowire faceting, ZB/WZ nanowires featured approximately hexagonal cross sections with six dominant {112}/{1100} side-facets (Figure 4a,b).^{22–24} The {112} and {1100} families are parallel. Toward the base of the nanowires, where more significant radial growth has occurred, ZB nanowires frequently have an undulated, or microfaceted appearance as in Figure 2b. There, alternating {001} and {111}, {111}A and {111}B, or {113} and {111} microfacets comprise overall {112} sidewalls (Figure 2b).²²

The six {112} facets are not all equivalent and can be subdivided into three {112}A and three {112}B facets.^{22,24} The lower surface energy, stable {112}B facets tend to be elongated compared to the {112}A facets (Figure 4a), so the nanowire cross section tends toward a triangular shape rather than a perfect hexagon, as reported previously for GaAs and GaP nanowires.^{22,24} This is thought to be a consequence of radial growth: under the high group V overpressure conditions in the growth window, radial growth occurs preferentially on the {112}A facets, which then grow out.^{22,24}

For WZ nanowires, the six side-facets are approximately equal in length due to the nonpolar nature of {1100} surfaces (Figure 4b). In a minority of highly tapered WZ nanowires, {1120} facets are observed at the nanowire base, although the remainder of the nanowire remains {1100}. Figure 4d illustrates the facets of such a nanowire. These {1120} surfaces are thought to evolve during kinetically limited radial growth on nanowire sidewalls, rather than during axial growth.²

For our nucleation model, we are primarily interested in facets in the vicinity of the nanowire growth front. The observed faceting behavior is partially driven by radial growth and yet gives an understanding of the possible nucleus facets at the nanoparticle–nanowire interface: the {112}/{1100}, {001}, {111}, and {113} families. We also consider other plausible low index facets, namely, the {110}

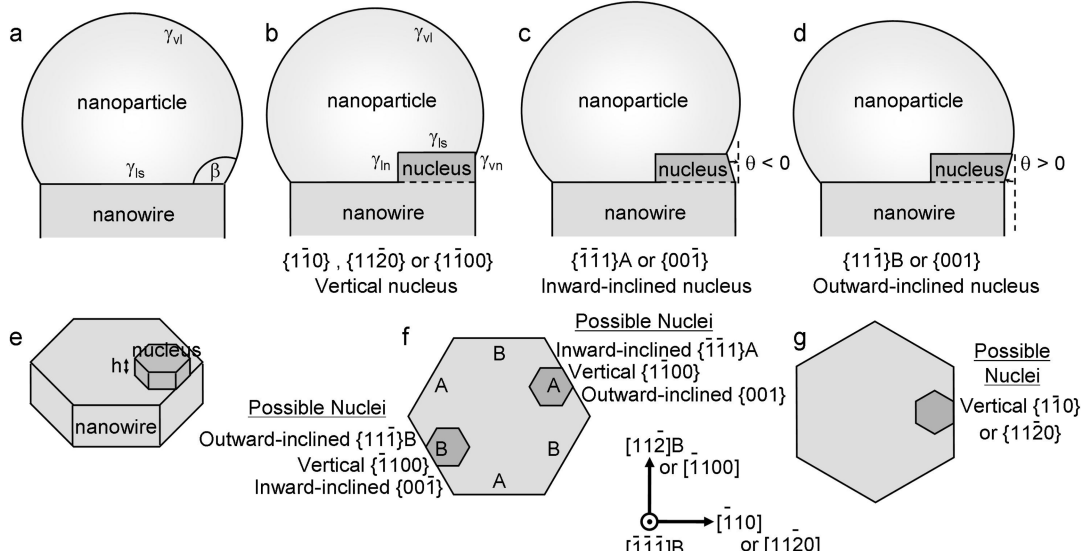


FIGURE 5. Schematic illustrations of the nucleus, liquid nanoparticle, and nanowire, indicating key parameters. (a) β is the contact angle of the liquid nanoparticle. (b) γ_{ln} , γ_{vn} , γ_{ls} , and γ_{vi} are the energies of the liquid–nucleus sidewall, vapor–nucleus, liquid–nucleus upper face, and vapor–liquid interfaces, respectively. The external nucleus facet is (b) vertical with $\theta = 0$, (c) inward-inclined with $\theta < 0$, and (d) outward-inclined with $\theta > 0$. (e) A hexagonal nucleus of bilayer height, h . (f, g) Possible nuclei on the different pre-existing side-facets. The labels A and B denote two types of nonequivalent side-facets.

and $\{1\bar{1}\bar{2}0\}$ facets, which have been reported for nanowires with significant radial growth or grown at high temperatures.^{2,25}

Our theoretical model builds on pre-existing models developed by several groups.^{12,14,17–19,26} These have established that III–V nanowires grow by repeated formation of two-dimensional nuclei on the nanoparticle–nanowire interface. Nucleation occurs at the three-phase contact line, where vapor, nanoparticle, and nanowire meet.^{14,18} Once a nucleus of critical size has formed, bilayer growth propagates over the remainder of the interface. Consider the nucleus illustrated in Figure 5, with height h (a single bilayer of III–V pairs).

Each nucleus creates a new external vapor–nucleus (v-n) facet at the three-phase contact line. Each nucleus (or bilayer) is named according to its v-n facet, for instance, as a $\{1\bar{1}\bar{1}\}A$ nucleus (or bilayer). The v-n facet makes an angle θ with the vertical and may be vertical as in Figure 5b ($\{1\bar{1}0\}$, $\{1\bar{1}\bar{2}0\}$, and $\{1\bar{1}00\}$ nuclei), inward-inclined as in Figure 5c ($\{1\bar{1}\bar{1}\}A$ and $\{001\}$ nuclei), or outward-inclined as in Figure 5d ($\{1\bar{1}\bar{1}\}B$ and $\{001\}$ nuclei). The $\{1\bar{1}\bar{2}0\}$ and $\{1\bar{1}00\}$ nuclei form with a twin plane, whereas the other nuclei do not involve a twin plane. This nomenclature is used to define the nuclei throughout this report.

We restrict our model to the six low index (singular) v-n facets: $\{1\bar{1}\bar{1}\}A$, $\{1\bar{1}\bar{1}\}B$, $\{001\}$, $\{1\bar{1}0\}$, $\{1\bar{1}00\}$, and $\{1\bar{1}\bar{2}0\}$. This gives a discrete set of six possible nuclei. Thus, each bilayer has a low index v-n facet. These bilayers are basic building blocks which can be constructed into higher index facets, such as $\{112\}$ and $\{113\}$.²⁷ Accordingly, $\{112\}A$ (or B) facets are comprised of a 2:1 ratio of $\{1\bar{1}\bar{1}\}A$ (or B) and $\{001\}$ bilayers, and $\{113\}A$ (or B) facets are

composed of alternating $\{1\bar{1}\bar{1}\}A$ (or B) and $\{001\}$ bilayers. This is illustrated in section S4 of the Supporting Information. High index facets possess physical and chemical characteristics in between those of their composite low index singular facets.²⁷ This further justifies a model of only low index facets.

According to EDX and TEM analysis, the nanoparticle is a polycrystalline Au–In alloy of hemispherical shape, as discussed in detail in section S7 of the Supporting Information. This suggests that during growth, nanoparticles were liquid. Accordingly, our model is derived for a liquid nanoparticle. The model is, nevertheless, also valid for solid particles which sinter or distort at the nanoparticle–nanowire interface.²¹

The enthalpy associated with nucleus formation is given by

$$\Delta G_t^* = \frac{b^2 h^2 \Gamma_t^2}{2c(\frac{\Delta\mu}{a} - \gamma_t)} \quad \text{and} \quad \Delta G^* = \frac{b^2 h^2 \Gamma^2}{2c \frac{\Delta\mu}{a}} \quad (1)$$

for nuclei with and without twins, respectively. In these equations, $\Delta\mu$ is the change in chemical potential per III–V pair, a is the area per III–V pair on the $\{1\bar{1}\bar{1}\}$ growth interface, γ_t is the twin formation energy, and b and c are geometric factors depending on the nucleus shape. The term Γ represents the total change in surface and interfacial energy due to nucleus formation, given by

$$\Gamma = (1 - \alpha)\gamma_{ln} + \alpha \left[\frac{\gamma_{vn}}{\cos \theta} + \gamma_{ls} \tan \theta + \gamma_{vl} \tan \theta \times \left(\frac{\beta \sin^3 \beta - \cos^3 \beta + 3 \cos \beta - 2}{(\cos \beta - 1)^2} \right) \right] \quad (2)$$

In this formula, β is the contact angle of the liquid nanoparticle, α is the fraction of nucleus perimeter in contact with the vapor, and γ_{ln} , γ_{vn} , γ_{ls} , and γ_{vl} are the energies of the liquid–nucleus sidewall, vapor–nucleus, liquid–nucleus upper face, and vapor–liquid interfaces, as illustrated in Figure 5. A complete derivation of eqs 1 and 2 is given in section S5 of the Supporting Information.

The formation of inclined nuclei causes a change in β , meaning distortion of the nanoparticle. The quantity Γ accounts for the distortion. Formation of outward-inclined nuclei (Figure 5d), for example, $\{11\bar{1}\}B$, causes the nanoparticle–nanowire interface to locally expand, the nanoparticle to be pulled taut, and β to decrease.¹² With continuing nucleation of outward-inclined $\{11\bar{1}\}B$ nuclei, β decreases further, until a critical angle β_c where $\Gamma_{\{11\bar{1}\}B}$ is large and another nucleus is favored. This nucleus is either an inward-inclined $\{00\bar{1}\}$ nucleus without a twin plane or a vertical $\{1\bar{1}00\}$ nucleus accompanied by a twin plane, which respectively relieve the distortion or prevent further distortion of the nanoparticle. The relative values of $\Gamma_{\{00\bar{1}\}}$ and $\Gamma_{\{1\bar{1}00\}}$ determine whether the nucleus is $\{00\bar{1}\}$ or $\{1\bar{1}00\}$. On the other hand, inward-inclined nuclei (Figure 5c), for example $\{1\bar{1}1\}A$, cause β to increase,¹² until $\Gamma_{\{1\bar{1}1\}A}$ is large and an outward-inclined $\{00\bar{1}\}$ nucleus, or a vertical $\{1\bar{1}00\}$ nucleus accompanied by a twin plane, become more energetically favorable. Parts f and g of Figure 5 illustrate the possible nuclei on each of the nonequivalent side-facets.

Then, following the approach of Johansson et al.,^{14,19} the probability of a twinned nucleus is given by

$$P_t = \exp\left(-\frac{\Delta G_t^*}{k_B T}\right) / \sum_i \exp\left(-\frac{\Delta G_{iy}^*}{k_B T}\right) \quad (3)$$

where k_B is the Boltzmann constant and T is the growth temperature (K). Pure ZB growth requires $P_t = 0$, and pure WZ growth requires $P_t = 1$. Section S5 of the Supporting Information gives a complete description of the model. Here we focus on how growth conditions affect the parameters in eqs 1 and 2 and, consequently, affect the probability of twin nucleation, which in turn determines the experimentally observed ZB to WZ growth transition. Using published data for InAs, we obtained estimates for the parameters in eqs 1 and 2. The twin formation energy, γ_t , takes into account the lattice parameter and ionicity of InAs.²⁸ This is estimated as approximately half the stacking fault energy, giving γ_t of 0.94 meV/Å².²⁹ The vapor–liquid surface energy γ_{vl} lies between the surface energies of pure Au and pure In

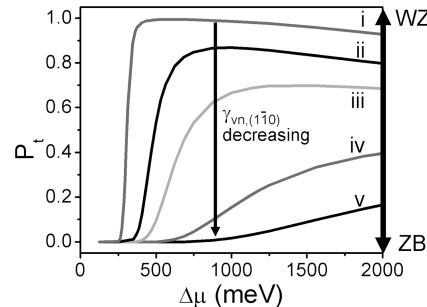


FIGURE 6. Twin probability, P_t , within the range of supersaturation $\Delta\mu$ relevant to the MOCVD growth system, as calculated by the model. This plot considers only vertical $\{11\bar{2}0\}$ and $\{1\bar{1}0\}$ nuclei. P_t is calculated assuming $\gamma_{vn(11\bar{2}0)} = 36 \text{ meV}/\text{\AA}^2$, its published value,³² and arbitrary values of $\gamma_{vn(1\bar{1}0)}$: (i) 48, (ii) 42, (iii) 40, (iv) 36, and (v) 32 $\text{meV}/\text{\AA}^2$.

and depends on the liquid composition.³⁰ We choose $\gamma_{vl} = 56 \text{ meV}/\text{\AA}^2$. At the $\{11\bar{1}\}B$ nanoparticle–nucleus interface, the surface energies γ_{ls} and γ_{ln} are approximated as the surface energy of a $\{11\bar{1}\}B$ surface,¹² $36 \text{ meV}/\text{\AA}^2$. Values for γ_{vn} are tabulated in Table S1 of the Supporting Information for each type of nucleus. We present results for a hexagonal nucleus shape and note that the trends we discuss pertain for all the other nuclear geometries we studied, including triangular, semicircular, or truncated circular.³¹

First, we consider the effect of $\Delta\mu$, and how it is influenced by temperature and V/I ratio. The chemical potential is a measure of the supersaturation of the growth system, and hence $\Delta\mu$ and supersaturation can be used interchangeably. In Figure 6 we plot P_t against $\Delta\mu$, considering the simplified scenario of twinned $\{11\bar{2}0\}$ and twin-free $\{1\bar{1}0\}$ nuclei. We use the published value³² of $\gamma_{vn(11\bar{2}0)} = 36 \text{ meV}/\text{\AA}^2$ and plot P_t for arbitrary values of $\gamma_{vn(1\bar{1}0)}$. Figure 6 indicates that twin nucleation and, consequently, a majority proportion of WZ phase are possible under certain growth conditions. First, Γ_t for twinned nuclei must be less than Γ for nontwinned nuclei. For $\{11\bar{2}0\}$ and $\{1\bar{1}0\}$ nuclei, this means the surface energies of WZ facets, $\gamma_{vn(11\bar{2}0)}$ must be lower than those of ZB facets, $\gamma_{vn(1\bar{1}0)}$, as for curves (i), (ii), and (iii). Second, the chemical potential, $\Delta\mu$, must be moderately high. In this plot, we considered vertical nuclei for simplicity. For inclined nuclei, the results are analogous, and $\Delta\mu$ must be moderately high for twin formation to occur at the critical angle β_c .

The relationship between $\Delta\mu$, growth temperature T , and the flows of group III and group V precursors is given by

$$\Delta\mu = k_B T \ln \frac{C_{In} C_{As}}{C_{In,eq} C_{As,eq}} \quad (4)$$

where C_x and $C_{x,eq}$ are the concentrations of reactant x during growth and at equilibrium with the InAs crystal, respectively. Group III species are expected to be supplied from the Au–In

alloy nanoparticle, so C_{In} and $C_{\text{In},\text{eq}}$ refer to the In concentrations in the alloy. Group V species, on the other hand, have very low solubility in Au and are expected to be supplied to the growth interface from the vapor phase, so C_{As} and $C_{\text{As},\text{eq}}$ refer to the vapor phase As concentrations.

According to eq 4, an increase in growth temperature, T , increases $\Delta\mu$. This in turn can promote WZ growth, as discussed for Figure 6. Our experimental results are consistent with this theoretical prediction and that of Johansson et al.: twin defects and WZ growth occur selectively under high temperature and high supersaturation conditions.^{14,19}

Yet, according to eq 4, a high group V flow rate, that is, a high C_{As} , should also increase $\Delta\mu$ and thereby promote a WZ phase. Intriguingly, our experimental results, as discussed earlier, show the exact opposite behavior.

To account for this unexpected result, we first considered changes in γ_{ls} and γ_{vl} that occur with changes in V/III ratio and the effect on P_t . For example, group V species can potentially act as surfactants to decrease γ_{ls} and γ_{vl} .^{16,33} Our modeling studies show that changes in γ_{ls} and γ_{vl} can account for changes in the twin period, consistent with the work of Algra et al.¹² Interestingly, changes in γ_{vl} may explain the results of Caroff et al. for InAs nanowires.¹³ According to their results, the twin period decreased with decreasing temperature, tending to WZ phase nanowires. With decreasing temperature, γ_{vl} increases, and this could be responsible for the shortened twin period observed by Caroff et al.¹³ The effects of γ_{ls} and γ_{vl} on twin period are further described in section S6 of the Supporting Information. However, our model reveals that γ_{ls} and γ_{vl} merely affect the twin period and cannot account for a complete transition from twin-free ZB to pure WZ.

Instead, we find that the critical factor, determining ZB and WZ phase perfection, is the change in γ_{vn} that occurs with temperature and V/III ratio. For many III–V semiconductors, surface energies can change markedly with temperature and V/III ratio.^{34–39} The surface energy is closely related to the surface reconstruction adopted under the growth conditions. Surface reconstructions consist of a discrete arrangement of surface atoms, into unit cells which periodically repeat over the surface. For instance, under high As overpressure, $\{1\bar{1}\}\text{B}$ surfaces can form an As trimer reconstruction.³⁹

For ZB structures, the surface reconstruction and surface energy of $\{1\bar{1}0\}$, $\{1\bar{1}\}\text{A}$, $\{1\bar{1}\}\text{B}$, and $\{001\}$ surfaces, can depend strongly on As overpressure, that is, the V/III ratio.^{37,38,40} At higher As flow rates, these surfaces adsorb As atoms onto the surface, to form energetically favorable surface reconstructions, such as the As trimers mentioned above. Surfaces composed of these low index planes, namely, $\{112\}$ and $\{113\}$ surfaces, also form low energy surface reconstructions under As-rich conditions.⁴¹ These low-energy As-stabilized surfaces are also stable at low temperature, where As desorption is minimal.^{34,38} In contrast, at low V/III ratios where As coverage is not possible, and at high

temperatures where As desorption is significant, these surface reconstructions cannot form and a higher energy surface reconstruction is adopted.

Wurtzite crystal surfaces, $\{11\bar{2}0\}$ and $\{1\bar{1}00\}$, show very different surface behavior to their ZB counterparts. These WZ surfaces are not believed to form low-energy surface reconstructions under high As pressure.³⁵ The $\{11\bar{2}0\}$ surfaces are unlikely to reconstruct or change surface energy significantly with growth conditions.^{32,35} It is possible that $\{1\bar{1}00\}$ surfaces form low-energy surface reconstructions under In-rich conditions, similar to GaN $\{1\bar{1}00\}$ surfaces under Ga-rich conditions.³⁵ These In-rich conditions, that is, high μ_{In} conditions, occur at high growth temperature and low V/III ratio. Under these conditions, In species can readily diffuse from the substrate and along the nanowire sidewalls for incorporation into the alloy nanoparticle, which increases μ_{In} .

The discussion above illustrates a trend, where the γ_{vn} of ZB nuclei ($\{1\bar{1}\}\text{A}$, $\{1\bar{1}\}\text{B}$, $\{001\}$, and $\{1\bar{1}0\}$) is lowest under conditions of high As coverage: high V/III ratio and low growth temperature. It is this trend that allows the formation of perfect twin-free nanowires at low temperature and high V/III ratio. Rather than a twinned $\{1\bar{1}00\}$ nucleus forming in response to nanoparticle deformation, a twin-free $\{001\}$ nucleus, with low γ_{vn} , can form. On the other hand, at higher temperatures and low V/III ratios, WZ nuclei ($\{11\bar{2}0\}$ or $\{1\bar{1}00\}$) are likely to have lower γ_{vn} than their ZB counterparts. Indeed, modeling within the range of possible γ_{vn} (Table S1 of the Supporting Information) reveals that changes in γ_{vn} are largely responsible for ZB and WZ phase purity (section S6 of the Supporting Information).

In conclusion, simply by tailoring the basic growth parameters of temperature and V/III ratio, we achieved pure ZB and pure WZ III–V nanowires. Thus, complete phase transitions can be achieved without compromising other key nanowire properties, such as diameter and doping. Indeed, the crystal phase could be tightly controlled over a wide range of nanowire diameters. Using a comprehensive model of nanowire nucleation, we established that the orientation and surface energy of the external vapor–nucleus facet determine the probability of twin formation. Changes to the vapor–nucleus surface energy, which occur with changes in growth conditions, are critical for achieving phase purity. A low temperature and high V/III ratio promote twin-free ZB growth. Under these growth conditions, ZB surfaces can form low-energy surface reconstructions, making the nucleation and growth of ZB nanowires more energetically favorable. The low temperature also creates a low supersaturation growth condition, which further hinders twin formation. In direct contrast, using high temperatures and low V/III ratios, conditions under which ZB surfaces are less stable, we achieved perfect, stacking fault-free WZ nanowires.

Acknowledgment. We thank the Australian Research Council for financial support and the Australian National Fabrication Facility established under the Australian Government's National Collaborative Research Infrastructure Strategy, for providing access to the facilities used in this research.

Supporting Information Available. Results for entire InAs nanowire lengths, for GaAs nanowires, and for other nanowire diameters, development and discussion of the ZB/WZ nucleation model, and a discussion of the Au nanoparticle composition and phase. This material is available free of charge via the Internet at <http://pubs.acs.org>.

REFERENCES AND NOTES

- (1) (a) Law, M.; Greene, L. E.; Johnson, J. C.; Saykally, R.; Yang, P. *Nat. Mater.* **2005**, *4*, 455–459. (b) Garnett, E. C.; Yang, P. *J. Am. Chem. Soc.* **2008**, *130*, 9224–9225.
- (2) Czaban, J. A.; Thompson, D. A.; LaPierre, R. R. *Nano Lett.* **2009**, *9*, 148–154.
- (3) (a) Huang, M. H.; Mao, S.; Feick, H.; Yan, H.; Wu, Y.; Kind, H.; Weber, E.; Russo, R.; Yang, P. *Science* **2001**, *292*, 1897–1899. (b) Duan, X. F.; Huang, Y.; Agarwal, R.; Lieber, C. M. *Nature* **2003**, *421*, 241–245.
- (4) (a) Chin, A. H.; Vaddiraju, S.; Maslov, A. V.; Ning, C. Z.; Sunkara, M. K.; Meyyappan, M. *Appl. Phys. Lett.* **2006**, *88*, 163115. (b) Hua, B.; Motohisa, J.; Kobayashi, Y.; Hara, S.; Fukui, T. *Nano Lett.* **2009**, *9*, 112–116.
- (5) Wang, J.; Gudiksen, M. S.; Duan, X.; Cui, Y.; Lieber, C. M. *Science* **2001**, *293*, 1455–1457.
- (6) Park, H.-G.; Barrelet, C. J.; Wu, Y.; Tian, B.; Qian, F.; Lieber, C. M. *Nat. Photonics* **2008**, *2*, 622–626.
- (7) Cui, Y.; Wei, Q.; Park, H.; Lieber, C. M. *Science* **2001**, *293*, 1289–1292.
- (8) Yi, S. S.; Girolami, G.; Amano, J.; Islam, M. S.; Sharma, S.; Kamins, T. I.; Kimukin, I. *Appl. Phys. Lett.* **2006**, *89*, 133121.
- (9) (a) Woo, R. L.; Xiao, R.; Kobayashi, Y.; Gao, L.; Goel, N.; Hudait, M. K.; Mallouk, T. E.; Hicks, R. F. *Nano Lett.* **2008**, *8*, 4664–4669. (b) Perera, S.; Fickenscher, M. A.; Jackson, H. E.; Smith, L. M.; Garrison-Rice, J. M.; Joyce, H. J.; Gao, Q.; Tan, H. H.; Jagadish, C.; Zhang, X.; Zou, J. *Appl. Phys. Lett.* **2008**, *93*, 053110. (c) Parkinson, P.; Joyce, H. J.; Gao, Q.; Tan, H. H.; Zhang, X.; Zou, J.; Jagadish, C.; Herz, L. M.; Johnston, M. B. *Nano Lett.* **2009**, *9*, 3349–3353.
- (10) (a) Bao, J.; Bell, D. C.; Capasso, F.; Wagner, J. B.; Mårtensson, T.; Trägårdh, J.; Samuelson, L. *Nano Lett.* **2008**, *8*, 836–841. (b) Mishra, A.; Titova, L. V.; Hoang, T. B.; Jackson, H. E.; Smith, L. M.; Garrison-Rice, J. M.; Kim, Y.; Joyce, H. J.; Gao, Q.; Tan, H. H.; Jagadish, C. *Appl. Phys. Lett.* **2007**, *91*, 263104. (c) Hoang, T. B.; Moses, A. F.; Zhou, H. L.; Dheeraj, D. L.; Fimland, B. O.; Weman, H. *Appl. Phys. Lett.* **2009**, *94*, 133105.
- (11) Shtrikman, H.; Popovitz-Biro, R.; Kretinin, A.; Houben, L.; Heiblum, M.; Bukala, M.; Galicka, M.; Buczko, R.; Kacman, P. *Nano Lett.* **2009**, *9*, 1506–1510.
- (12) Algra, R. E.; Verheijen, M. A.; Borgstrom, M. T.; Feiner, L.-F.; Immink, G.; van Enckevort, W. J. P.; Vlieg, E.; Bakkers, E. P. A. M. *Nature* **2008**, *456*, 369–372.
- (13) Caroff, P.; Dick, K. A.; Johansson, J.; Messing, M. E.; Deppert, K.; Samuelson, L. *Nat. Nanotechnol.* **2009**, *4*, 50–55.
- (14) Johansson, J.; Karlsson, L. S.; Svensson, C. P. T.; Mårtensson, T.; Wacaser, B. A.; Deppert, K.; Samuelson, L.; Seifert, W. *Nat. Mater.* **2006**, *5*, 574–580.
- (15) Joyce, H. J.; Gao, Q.; Tan, H. H.; Jagadish, C.; Kim, Y.; Zhang, X.; Guo, Y.; Zou, J. *Nano Lett.* **2007**, *7*, 921–926.
- (16) Joyce, H. J.; Gao, Q.; Tan, H. H.; Jagadish, C.; Kim, Y.; Fickenscher, M. A.; Perera, S.; Hoang, T. B.; Smith, L. M.; Jackson, H. E.; Garrison-Rice, J. M.; Zhang, X.; Zou, J. *Adv. Funct. Mater.* **2008**, *18*, 3794–3800.
- (17) Hurle, D. T. *J. Cryst. Growth* **1995**, *147*, 239–250.
- (18) Glas, F.; Harmand, J. C.; Patriarche, G. *Phys. Rev. Lett.* **2007**, *99*, 146101.
- (19) Johansson, J.; Karlsson, L. S.; Dick, K. A.; Bolinsson, J.; Wacaser, B. A.; Deppert, K.; Samuelson, L. *Cryst. Growth Des.* **2009**, *9*, 766–773.
- (20) Dayeh, S. A.; Yu, E. T.; Wang, D. *Nano Lett.* **2007**, *7*, 2486–2490.
- (21) Persson, A. I.; Larsson, M. W.; Stenström, S.; Ohlsson, B. J.; Samuelson, L.; Wallenberg, L. R. *Nat. Mater.* **2004**, *3*, 677–681.
- (22) Verheijen, M. A.; Algra, R. E.; Borgstrom, M. T.; Immink, G.; Sourty, E.; van Enckevort, W. J. P.; Vlieg, E.; Bakkers, E. P. A. M. *Nano Lett.* **2007**, *7*, 3051–3055.
- (23) Johansson, J.; Wacaser, B. A.; Dick, K. A.; Seifert, W. *Nanotechnology* **2006**, *17*, S355.
- (24) Zou, J.; Paladugu, M.; Wang, H.; Auchterlonie, G. J.; Guo, Y.; Kim, Y.; Gao, Q.; Joyce, H. J.; Tan, H. H.; Jagadish, C. *Small* **2007**, *3*, 389–393.
- (25) Skold, N.; Wagner, J. B.; Karlsson, G.; Hernan, T.; Seifert, W.; Pistol, M.-E.; Samuelson, L. *Nano Lett.* **2006**, *6*, 2743–2747.
- (26) Ross, F. M.; Terhoff, J.; Reuter, M. C. *Phys. Rev. Lett.* **2005**, *95*, 146104.
- (27) Nötzel, R.; Däweritz, L.; Ploog, K. *Phys. Rev. B* **1992**, *46*, 4736–4743.
- (28) Ito, T. *Jpn. J. Appl. Phys.* **1998**, *37*, L1217–L1220.
- (29) Gottschalk, H.; Patzer, G.; Alexander, H. *Phys. Status Solidi A* **1978**, *45*, 207–217.
- (30) Schwalbach, E. J.; Voorhees, P. W. *Nano Lett.* **2008**, *8*, 3739–3745.
- (31) van Enckevort, W. J. P. *J. Cryst. Growth* **2003**, *259*, 190–207.
- (32) Hilner, E.; Häkanson, U.; Fröberg, L. E.; Karlsson, M.; Kratzer, P.; Lundgren, E.; Samuelson, L.; Mikkelsen, A. *Nano Lett.* **2008**, *8*, 3978–3982.
- (33) Joyce, H. J.; Gao, Q.; Tan, H. H.; Jagadish, C.; Kim, Y.; Fickenscher, M. A.; Perera, S.; Hoang, T. B.; Smith, L. M.; Jackson, H. E.; Garrison-Rice, J. M.; Zhang, X.; Zou, J. *Nano Lett.* **2009**, *9*, 695–701.
- (34) (a) Moison, J. M.; Guille, C.; Bensoussan, M. *Phys. Rev. Lett.* **1987**, *58*, 2555–2558. (b) Ohkouchi, S.; Ikoma, N. *Jpn. J. Appl. Phys.* **1994**, *33*, L1700–L1702.
- (35) Northrup, J. E.; Neugebauer, J. *Phys. Rev. B* **1996**, *53*, R10477–R10480.
- (36) Pehlke, E.; Moll, N.; Kley, A.; Scheffler, M. *Appl. Phys. A: Mater. Sci. Process.* **1997**, *65*, 525–534.
- (37) (a) Ratsch, C.; Barvosa-Carter, W.; Grosse, F.; Owen, J. H. G.; Zinck, J. J. *Phys. Rev. B* **2000**, *62*, R7719–R7722. (b) Moll, N.; Kley, A.; Pehlke, E.; Scheffler, M. *Phys. Rev. B* **1996**, *54*, 8844–8855.
- (38) Miwa, R. H.; Srivastava, G. P. *Phys. Rev. B* **2000**, *62*, 15778–15787.
- (39) Taguchi, A. *J. Cryst. Growth* **2005**, *278*, 468–472.
- (40) Schmidt, W. G. *Appl. Phys. A: Mater. Sci. Process.* **2002**, *75*, 89–99.
- (41) (a) Kawase, M.; Ishikawa, Y.; Fukui, T. *Appl. Surf. Sci.* **1998**, *130–132*, 457–463. (b) Jacobi, K.; Geelhaar, L.; Márquez, J.; Platen, J.; Setzer, C. *Appl. Surf. Sci.* **2000**, *166*, 173–178.